Enhanced electrochemical performance of electrospun V_2O_5 fibres doped with redox-inactive metals

Ceilidh F. Armer[1,2], Mechthild Lübke[2,3], Ian Johnson[3], Kit McColl[3], Furio Cora[3], Joyce S. Yeoh[1], M. V. Reddy[4,5], Jawwad A. Darr[3], Xu Li[2]*, Adrian Lowe[1]*

[1] College of Engineering and Computer Science, Australian National University, Canberra, ACT 0200, Australia
[2] Institute of Materials Research and Engineering, Agency for Science, Technology and Research (A*STAR), 2 Fusionopolis Way, Innovis #08-03, Singapore 138634, Singapore
[3] Department of Chemistry, University College London, 20 Gordon Street, London, WC1H 0AJ, UK
[4] Department of Physics, National University of Singapore, Singapore 117542, Singapore
[5] Department of Materials Science and Engineering, National University of Singapore, Singapore 117576, Singapore

*Corresponding authors: Dr Adrian Lowe,
College of Engineering and Computer Science, Australian National University
Canberra, ACT 0200
Office telephone: +61 2 6125 4881,Email: adrian.lowe@anu.edu.au; Dr Xu Li, Office telephone: +65 6416 8933, Email: x-li@imre.a-star.edu.sg

Acknowledgements

The authors thank the A*STAR Research Attachment Program, Institute of Materials Research and Engineering (IMRE), Singapore. Thanks to Professor B V R Chowdari, National University of Singapore Department of Physics, for the use of his laboratories in processing these coin cells. Further thanks to Luxmi Devi Narain for graphical support. The authors acknowledge the use of the UCL Legion High Performance Computing Facility (Legion@UCL), and associated support services, in the completion of this work.

Abstract

The structural and electrochemical effects of electrospun V_2O_5 with selected redox-inactive dopants (namely Na^+, Ba^{2+}, and Al^{3+}), have been studied. The electrospun materials have been characterised *via* a range of analytical methods including X-ray diffraction, X-ray photoelectron spectroscopy, Brunauer-Emmett-Teller surface area measurements, scanning and transmission electron microscopy. The incorporation of dopants in V_2O_5 was further studied with computational modelling. Structural analysis suggested that the dopants had been incorporated into the V_2O_5 structure with changes in crystal orientation and particle size, and variations in the V^{4+} concentration. Electrochemical investigations using potentiodynamic, galvanostatic and impedance spectroscopy analysis, showed that electrochemical performance might be dependent on V^{4+} concentration, which influenced electronic conductivity. Na^+ or Ba^{2+} doped V_2O_5 offered improved conductivities and lithium ion diffusion properties, while Al^{3+} doping was shown to be detrimental to these properties. The energetics of dopant incorporation, calculated using atomistic simulations, indicated that Na^+ and Ba^{2+} occupy interstitial positions in the interlayer space, while Al^{3+} is incorporated in V sites and replaces a vanadyl-like $(VO)^{3+}$ group. Overall, the mode of incorporation of the dopants affects the concentration of oxygen vacancies and V^{4+} ions in the compounds, and in turn their electrochemical performance.

Highlights

1. Dopants of varying oxidation states incorporated into electrospun V_2O_5 are studied.
2. Doping showed significant impacts on the crystallinity and V^{4+} concentration.
3. 2 at% Na^+ and 3 at% Ba^{2+} in V_2O_5 improved electrochemical performance.
4. Doping 3 at% Al^{3+} in V_2O_5 did not improve electrochemical performance.

Key Words

lithium ion battery; positive electrode; electrospinning; V_2O_5; doping

Graphical Abstract

1. Introduction

The development of energy storage technologies such as Li-ion batteries (LIBs), is of great interest in a range of applications from consumer electronics to transport [1]. Higher energy-density and cycle life LIBs are required for emergent technologies, such as e-bikes or full electric vehicles, but these are currently limited by the energy density and electrochemical performance of the available electrode materials. Therefore, the development of new electrode materials for LIBs, which are reliable, structurally stable and possess high cycle stability, is imperative to advance the state-of-the-art LIB technology.

Vanadium pentoxide is a promising candidate electrode material for energy storage due to its layered structure and controllable oxidation states that can reversibly intercalate lithium (Li) ion charge carriers [2]. The first report of Li-ion intercalation into V_2O_5 by Whittingham occurred in 1976 [3] though more recently there has been renewed interest as an electrode material due to synthesis of novel nano-scale morphologies such as nanofibres, hollow spheres and nanorods [4–6]. The crystalline variant of the V_2O_5 structure is formed from pairs of orthorhombic V_2O_5 layers consisting of distorted VO_5 square pyramids, in an up-up-down-down arrangement across an interlayer distance of approximately 4.4 Å in a near perfect bilayer arrangement [7, 8]. The structure contains a particularly short V-O bond perpendicular to the layer orientation that behaves as a vanadyl-like unit. The amorphous variant, bilayered $V_2O_5.nH_2O$, also consists of distorted VO_5 pyramids though are all facing the same direction. This monoclinic structure contains water that produces a large interlayer distance of 8 Å and often exists as xerogels or aerogels [9, 10].

Crystalline V_2O_5 undergoes a series of well-defined phase changes when intercalating Li-ions in the range of 2.0 to 4.0 V vs Li/Li^+, which are explained in detail elsewhere [5,8–11]. Despite the research interest shown in vanadium oxide materials for LIBs, poor structural stability and low electronic and ionic conductivities, impair the cycle life and electrode kinetics [2, 15], although addition of dopants can partially overcome these limitations [16].

As previously shown, redox-inactive dopants can improve the energy storage characteristics of vanadium containing host active materials [17–20]. Doping 9 at% Al^{3+} into V_2O_5 improved electrochemical cycling stability, which was attributed to increased cohesion between the weakly bonded V_2O_5 bilayers [21]. XPS revealed that a combination of V^{4+} and V^{5+} species are present for 20 and 33 at% Al^{3+} doped V_2O_5 materials; Raman spectroscopy suggested that the Al^{3+} ions formed AlO_6 octahedra by associating with the oxygens of neighbouring VO_5 square pyramidal units [22]. A previous study described the phase change effects of electrospun V_2O_5 doped with *ca*. 10 at% redox inactive dopants, Ba^{2+} or Ti^{4+} [23]. It was found that the cycle stability of the doped V_2O_5 was improved compared to undoped V_2O_5 in both cases, and additionally that the Ti^{4+} dopant resulted in increased charge storage capacity. The lack of increased capacity for the Ba^{2+}-doped V_2O_5 was attributed to active site blockage within the V_2O_5 layers. Liu *et al*. reported that NaV_6O_{15} nanorods prepared through hydrothermal synthesis, possessed a tunnel structure consisting of a $(V_2O_5)_x$ framework with Na^+ aligned along the *b* axis (which allowed for high mobility of foreign species such as Li-ions) [24]. The NaV_6O_{15} nanorods were heat-treated at 300, 400 and 500 °C, and XRD data suggested an improvement in crystallinity and electrochemical performance with increased processing temperature. The improved capacities were partly attributed to the mobility of the Li-ions along these tunnels in addition to the partial substitution of Na^+ with Li-ions, which was confirmed by X-ray photoelectron spectroscopy (XPS). XPS also showed that both V^{5+} and V^{4+} species were present before and after cycling, which demonstrated the integrity of the NaV_6O_{15} structure.

Whilst studying the electrochemical performance of doped V_2O_5, several reports have emphasised the importance of increasing the V^{4+} content and number of oxygen vacancies caused by the introduction of dopants. Coustier *et al.* found that doping V_2O_5 xerogels with Ag^+ increased conductivity, which was partially due to an increase in V^{4+} sites and the associated increase in polaron hopping [25, 26]. Higher electronic conductivities were attributed to the presence of V^{4+} in a range of other doped V_2O_5 compounds: (i) Cr^{3+} doped V_2O_5 at both 2 and 5 at% loadings [27], (ii) 2 at% Cu^{2+} doped V_2O_5 [28], and (iii) 3 at% loading for Gd^{3+} or Nd^{3+} doped V_2O_5 [29]. Furthermore, whilst the exact dopant level was not specified in terms of a molar ratio, a similar observation was made for Fe^{3+} doped V_2O_5 with

three different loadings [30]. Improved electrochemical performance of V_2O_5 in terms of increased Li-ion mobility has been attributed to an increased V^{4+} content with increased preinserted Na^+ (0.5, 1, or 2 at%) into V_2O_5 [31]. The presence of both V^{4+} and oxygen vacancies in 4 at% Sn^{4+} doped V_2O_5 was responsible for improved Li-ion mobility according to Li *et al* [32].

Although dopants have been demonstrated to modify the V_2O_5 properties, determining the precise location of the dopants is often challenging. Given the open structure of V_2O_5,incorporation in the interstitial space between the layers is generally stated as the likely location (inferred from changes in interlayer spacing) [21, 33]. Giorgetti *et al.* used X-ray absorption spectroscopy (XAS) to investigate the position of Cu^{2+} and Zn^{2+} dopants in V_2O_5 aerogels, concluding that dopants either occupied the space between the V_2O_5 bilayers or they sat close to a single layer [34]. It has been suggested that the dopants that sit between the bilayers block active sites for Li-ion interaction, and hence do not contribute towards a higher capacity compared to the undoped material. Dopants that sit closer to one of the single layers, appear to still allow movement of Li-ions while simultaneously offering improved structural stability and improved capacities. In crystalline V_2O_5, exhibiting an interlayer d-spacing of approximately 4.4 Å [10, 34, 35], cationic dopants can in principle occupy not only interstitial sites between the V_2O_5 layers, but also substitutional sites by replacing V^{5+} ions. The presence of the dopants requires additional defects to ensure charge balance, whose nature and concentration is likely to depend on the type of dopant employed.

Herein, Na^+-, Ba^{2+}- and Al^{3+}-doped V_2O_5 materials were synthesised *via* electrospinning, which is an effective and inexpensive nano-fabrication method that can produce high aspect ratio fibrous materials with controllable morphologies. This method is explained in detail elsewhere [1]. The V_2O_5 produced in this study is crystalline. In brief, electrospinning allows the production of metal oxide fibres with a dopant material (added to the starting solution prior to electrospinning) [20]. The process is flexible and could also allow incorporation of carbon derivatives into the electrospun fibres [36]. Electrospun undoped V_2O_5 has been synthesised and investigated by several groups for energy storage purposes [21–25]. Determining the location of dopants is challenging experimentally and we have used computational atomistic simulation techniques to investigate the energetics for substitutional and

interstitial Na^+, Ba^{2+} and Al^{3+} ions, to determine their likely positions in the V_2O_5 lattice and help rationalize the electronic conductivity and electrochemical behavior of the doped systems observed experimentally.

2. Experimental Section

1. Materials

The electrospinning starting solution contained vanadium oxytripropoxide (98%, Sigma-Aldrich, Castle Hill, Australia), ethanol (96%, Chem-Supply, Gillman Australia), and polyvinyl acetate (PVAc, Mw 140,000; Sigma-Aldrich, Castle Hill, Australia). Na^+ was introduced *via* the addition of sodium acetate (98%, Sigma-Aldrich, Thomastown, Australia), Ba^{2+} *via* barium oxide (90%, Fisher Scientific (Ajax Finechem) Tarren Point, Australia), and Al^{3+} *via* aluminium isopropoxide (98%, Sigma-Aldrich, Castle Hill, Australia). No further purification of the used chemicals was undertaken.

2. Synthesis of electrospun vanadium oxide fibres

The sol-gel was made up of 0.3 g of PVAc fully dissolved in 1.0 g of vanadium oxytripropoxide and 1.0 g of ethanol which formed a viscous orange solution. To introduce the Na^+ dopant, 0.0067 g of sodium acetate was added to the vanadium oxide sol-gel and stirred until a homogeneous mixture was obtained. For the Ba^{2+} dopant, 0.0126 g of barium oxide was added and for the Al^{3+} dopant, 0.017 g of aluminium isopropoxide. The Na^+ solution was dark orange and transparent in appearance, conversely, the Ba^{2+} and Al^{3+} solutions were both cloudy yellow suspensions. The solution was electrospun from a 5 mL syringe in a syringe pump (KD Scientific 78-9100 KDS-100-CE) with a feed a rate of 2 mL h^{-1} and a potential of 22 kV applied to the needle tip. The as-spun fibres were deposited on an aluminium foil collector and after collection, were heat treated at 500 °C for 2 h with a heat ramp rate of 3 C min^{-1} (furnace: SEM, SA Pty Ltd Cat No 1022).

3. Characterisation

Powder X-ray Diffraction (PXRD) of the electrospun fibers were collected using a Stoe StadiP diffractometer with Mo-Kα in transmission mode (Debye-Scherrer geometry), with the sample inserted into a 0.3 mm borosilicate glass capillary. Patterns were typically collected in the 2θ range of 2 to 60°, using a step size of 0.5° in 2θ and a collection time of 20 s per step. V_2O_5 reference XRD data was supplied by the Inorganic Crystal Structures Database (ICSD) (collection code 60767) with space group *Pmmn*(59) and the following unit cell parameters; a = 11.512 Å, b = 3.564 Å, and c = 4.368 Å. The unit cell parameters of the electrospun fibres were determined *via* Rietveld refinement using MAUD software [41] to reduce R_{wp} and χ^2_{XRD} with the previously mentioned space group and unit cell parameters as baselines. The unit cell was optimisation to reduce the R_P, R_{WP} and χ^2_{XRD} parameters. Apparent crystallite sizes were calculated using the Scherrer equation.

Surface composition and oxidation state determination of the elements were measured using a Thermo Scientific K-Alpha X-ray photoelectron spectrometer (XPS) fitted with a monochromatic Al-Kα source. CasaXPS^{TM} (version 2.3.16) software was used to fit the XPS data with the binding energies suited to oxygen (530.0 eV). Scanning electron microscope (SEM) images and energy dispersive X-ray spectroscopy (EDS) point analysis of the microfibers were taken with a JOEL FESEM JSM6700F to determine the morphology, fibrosity, grain structure, and dopant amount concentration. Fiber dimensions were determined using ImageJ *via* pixel counting. The morphology and size of the crystallites that made up with fibres were determined by transmission electron microscopy (TEM) using a JEOL JEM 2100 – LaB_6 filament. The TEM images were obtained using a Gatan Orius digital camera. Sample preparation involved dispersion in methanol followed by sonication and pipetting on a 300 mesh copper film grid (Agar Scientific). Before surface measurements were taken, using Brunauer-Emmett-Teller (BET) measurements with N_2 in a Micromeritics TriStar II 3012 analyser, the powders were degassed at 120 °C for12 h under vacuum.

The atomistic simulations investigating the incorporation energetics for substitutional and interstitial Na^+, Ba^{2+} and Al^{3+} ions in this report were conducted using empirically-fitted pair-potential methods. These methods are well established for the investigation of dopants in battery electrode materials, and are discussed in detail elsewhere [42, 43]. The procedure is described in more depth in the

Supplementary Section 2. All calculations were performed using the General Utility Lattice Program (GULP) [44].

4. Electrochemical Testing

For electrochemical testing, the vanadium oxide fibres were incorporated into positive electrodes and processed into CR2032-type coin cells. The working electrode consisted of 80 wt% active material, 10 wt% polyvinylidene fluoride (PVDF, Kynar 761) and 10 wt% conductive agent (carbon black, Super P 004, MMM Carbon). The PVDF was initially dissolved in N-methyl pyrrolidinone (NMP, Sigma Aldrich) followed by the addition of the active material and conductive agent. After vigorous hand mixing using a mortar and pestle, the slurry was doctor-bladed onto aluminium foil and dried at 70 °C for 1 h. Electrode discs were cut out with 16 mm diameters, pressed with 1 ton of force and dried overnight at 70 °C. The active material mass loadings in the working electrodes were 3.4 ± 0.2 mg cm^{-2}.

The prepared working electrodes were processed into coin cells in an argon-filled glove box (MBraun) in which oxygen and water levels were kept below 3 ppm. The counter and reference electrode was lithium foil (Hohsen Corp) with separators (glass microfiber filters, Whatman®, GF/B) soaked in an electrolyte consisting of 1 M $LiPF_6$ dissolved in a 1:1 v/v ratio of ethylene carbonate/dimethyl carbonate (EC/DMC) (Merck Selectipur LP40).

Cyclic voltammetry (CV) was conducted to investigate the electrochemical performance with a scan rate of 0.1 mV s^{-1} in the potential range over 2.0 to 4.0 V vs Li/Li^+ using a potentiostat (PGSTAT302, AUTOLAB, Metrohm). A MACCOR battery tester (Model 4200) was used to conduct C-rate tests and long-term cycling performance of the cells at 50, 100, 300, and 600 mA g^{-1} for 10 cycles each. Immediate following the cells were cycled at 50 mA g^{-1} for 60 cycles. Electrical impedance spectroscopy (EIS) measurements were performed on a Bio-Logic VMP3 potentiostat over 100 kHz – 100 mHz at the open circuit voltage (≈ 3.4 V vs Li/Li^+) with an AC amplitude of 20 mV on pristine coin cells. Nyquist plots and equivalent circuit determination were derived using the Zfit curve fitting function available in the EC-Lab® V10.33 software.

3. Results and discussion

1. Structure and Morphology

The samples are named accordingly; 2%Na^{+}-V_2O_5, 3%Ba^{2+}-V_2O_5 and 3%Al^{3+}-V_2O_5, as detailed in the XPS and EDS section.

The PXRD patterns in Figure 1(a) show that α-V_2O_5 was formed *via* electrospinning followed by heat treatment with the space group P*mmn* (ICSD collection code 60767) and reflection labelling for orthorhombic V_2O_5 according to Shklover *et al.* [45]. There are multiple impurity peaks detected in the PXRD pattern for 2%Na^{+}-V_2O_5, highlighted with asterisks, that are attributed to NaV_6O_{15} [46]. Rietveld refinement estimated that the molar ratio of V_2O_5:NaV_6O_{15} is 0.94:0.06, the calculation from the molar ratio is in Supplementary Section 1, it is reasonable to expect that the impurity may affect the electrochemical performance. No impurity peaks in the PXRD patterns for 3%Ba^{2+}-V_2O_5 and 3%Al^{3+}-V_2O_5 indicate that these dopants form a stable solid solution [47]. Additionally, there was a variation in material colour produced where undoped V_2O_5 was yellow, 2%Na^{+}-V_2O_5 appeared dark green/yellow, 3%Ba^{2+}-V_2O_5 was orange and 3%Al^{3+}-V_2O_5 was bright yellow as shown in Figure 1(a) inset. Furthermore, Figure 1(b,c) shows that there is little peak shifting and broadening between the XRD data of the different samples.

Figure 1: (a) PXRD patterns for V_2O_5, 2%Na^+-V_2O_5, 3%Ba^{2+}-V_2O_5, and 3%Al^{3+}-V_2O_5 with impurity peaks highlighted with asterisks for NaV_6O_{15} and (inset) a photo showing how colour of heat treated powder is affected by the dopant. Enlarged 2θ ranges (b) 8.5 to 10.5° and (c) 11.8 to 12.1°, emphasising intensity variations and the lack of peak shifts.

Table 1(a) summarises the Rietveld refined unit cell parameters and resultant unit cell volumes for each material, where the fitted patterns can be found in Figure S1. The unit cell volumes calculated for different samples were not particularly varied, which was likely to be due to the low doping levels used. The unit cell volume for 2%Na^+-V_2O_5 was the smallest, which may be related to the NaV_6O_{15} impurity producing a breakdown or altering of the V_2O_5 unit cell. Conversely, 3%Ba^{2+}-V_2O_5 had the largest unit cell volume, which was likely due to the size of Ba^{2+} as it is significantly larger than that of any of the other dopants [with an ionic radius of 1.35 Å and a coordination number (CN) of 6 compared to 1.00 Å for CN of 5 for Na^+, 0.48 Å for CN of 5 for Al^{3+} and 0.46 Å for CN of 5 for V^{5+}]. Additionally, the *c* parameter was the largest out of the investigated materials implying that large Ba^{2+} dopant distorted the

V_2O_5 unit cell. Cheah *et al.* observed an increase in the *a* and *c* parameters of Al^{3+} incorporated into V_2O_5 [22], whereas 3%Al^{3+}-V_2O_5 in this study displayed increased *c* and reduced *a* parameters (suggesting a different Al^{3+} dopant location in this sample).

Table 1: Characterisation summary: (a) Rietveld refinements of the lattice parameters with unit cell volumes, (b) crystallite size determined *via* the Scherrer equation, (c) the vanadium oxidation state ratios, V^{4+}:V^{5+} identified *via* XPS measurements, (d) specific surface area determined *via* BET surface area measurements.

			a				b	c	d
Sample	*a* (Å)	*b* (Å)	*c* (Å)	*V* (Å^3)	R_{wp} (%)	χ^2_{XRD}	Crystallite size (nm)	V^{4+}:V^{5+} ratio	Surface area (m^2 g^{-1})
V_2O_5	11.5210(3)	3.56773(9)	4.37694(12)	179.909(14)	9.59	1.48	36.1	0.08:0.92	8.70
2%Na^+-V_2O_5	11.5223(2)	3.56754(7)	4.37513(9)	178.846(10)	7.53	1.05	47.9	0.11:0.89	11.80
3%Ba^{2+}-V_2O_5	11.5205(3)	3.56719(8)	4.37950(11)	179.979(13)	8.81	1.32	42.1	0.09:0.91	14.30
3%Al^{3+}-V_2O_5	11.5197(3)	3.56687(1)	4.37905(14)	179.932(16)	8.45	1.17	36.5	0.02:0.98	22.18

The Scherrer equation was used to calculate apparent crystallite size using the average of the (200), (010), (101) and (400) peaks with estimates of 36.1 nm for undoped V_2O_5, 47.9 nm for 2%Na^+-V_2O_5, 42.1 nm for 3%Ba^{2+}-V_2O_5 and 36.5 nm for 3%Al^{3+}-V_2O_5 as summarised in Table 1(b). The crystal sizes are likely to be influenced by the dopant ion which might have affected crystal growth.

The oxidation states of the dopants were assigned in Figure 2 using the Na 1s [46], Ba $3d_{5/2}$ [48] and Al 2p peaks [49], whilst the ratio of the oxidation states for the vanadium was assigned using the V $2p_{3/2}$ peak. Analysis of the vanadium XPS data in Figure 3 showed a V^{4+}:V^{5+} ratio of 0.08:0.92 for V_2O_5, 0.11:0.89 for 2%Na^+-V_2O_5, 0.09:0.91 for 3%Ba^{2+}-V_2O_5 and 0.02:0.98 for 3%Al^{3+}-V_2O_5, also listed in Table 1(c). The Na^+:V atomic ratio according to the XPS analysis for 2%Na^+-V_2O_5 was 2:98 which agreed reasonably well with 3:97 indicated by EDS. For 3%Ba^{2+}-V_2O_5 the Ba^{2+}:V ratio was 3:97 (EDS indicated 2:98) and 3%Al^{3+}-V_2O_5 the Al^{3+}:V ratio was 2.5:97.5 (EDS indicated 3:97).

Figure 2: XPS elemental scans of the (a) V $2p_{3/2}$ peak for undoped V_2O_5, (b) V $2p_{3/2}$ peak and the Na 1s peak (inset) for 2%Na^+-V_2O_5, (c) V $2p_{3/2}$ peak and the Ba $3d_{5/2}$ peak (inset) for 3%Ba^{2+}-V_2O_5 and (d) the V $2p_{3/2}$ peak and the Al 2p peak (inset) for 3%Al^{3+}-V_2O_5.

The SEM images in Figure S2 revealed that the electrospun hierarchical fibres in this study were of consistent diameters and made up nanostructured particles. TEM images in Figure 3 confirmed that the electrospun fibres were made up of nanoscale particles that were of high crystallinity as evidenced by detectable lattice spacings. Figure 3(a-c) and Figure 3(d-f) showed similar morphologies for V_2O_5 and 2%Na^+-V_2O_5, respectively. These particles are elongated with lengths *ca.* 400 nm for V_2O_5 and up to several hundred nanometres for 2%Na^+-V_2O_5, suggesting directional growth during particle formation. V_2O_5 possessed well-defined lattice spacings of approximately 0.34 nm corresponding to (101) [Figure 3(c)]. The 2%Na^+-V_2O_5 material had particularly well-defined lattice spacings of 0.44 nm for (010) in

Figure 3(f). The addition of Ba^{2+} or Al^{3+} resulted in differing morphologies with rounder particles possessing diameters of *ca.* 400 nm for 3%Ba^{2+}-V_2O_5 [Figure 3(g)] and *ca.* 120 nm for 3%Al^{3+}-V_2O_5 [Figure 3(j)]. Two lattice planes are observable for 3%Ba^{2+}-V_2O_5 which are approximately 0.44 nm for (010) and 0.34 nm corresponding to the less defined (101) plane in Figure 3(i). For 3%Al^{3+}-V_2O_5, the (101) plane is observed with approximate 0.34 nm spacings in Figure 3(l). The interplanar spacings are well matched to the relevant XRD reflections

BET surface area measurements, according to Table 1(d), showed that for undoped V_2O_5 and 2%Na^{+}-V_2O_5, 3%Ba^{2+}-V_2O_5 and 3%Al^{3+}- $V_2O_5$the resultant surface areas were 8.7, 11.8, 14.3 and 22.2 m^2 g^{-1}, respectively, indicating that the presence of a dopant influenced not only the structural characteristics as seen in the XRD refinements but also the surface area. The doped materials seem to favour particle nucleation rather than Ostwald ripening and growth resulting in higher surfaces areas.

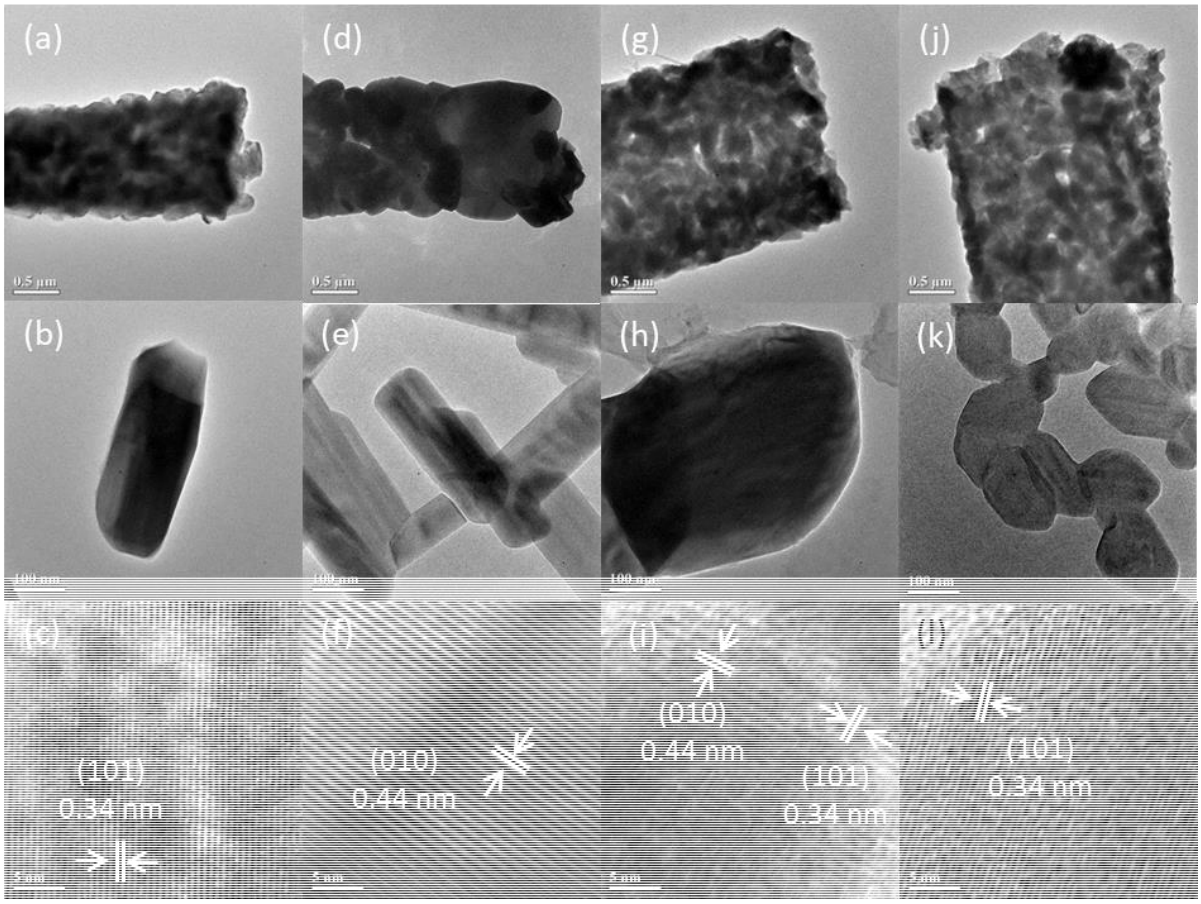

Figure 3: TEM images showing the microfiber in the first row, single particles in the second and lattice spacings *via* HRTEM in the third for (a-c) undoped V_2O_5, (d-f) 2%Na^+-V_2O_5, (g-i) 3%Ba^{2+}-V_2O_5 and (j-l) 3%Al^{3+}-V_2O_5, respectively.

2. Electrochemical performance

In Figure 4 the cyclic voltammetry (CV) results were conducted at 0.1 mV s^{-1} over two cycles within the potential range 2.0 to 4.0 V vs Li/Li^+. Each material showed clearly defined redox peaks indicating intercalation corresponding to two Li-ions per formula unit (i.e. 1 per V ion). One Li-ion intercalation process occurred in the range *ca.* 3.0 to 3.5 V vs Li/Li^+ which corresponded to the formation of δ-LiV_2O_5 from the unintercalated phase α-V_2O_5 *via* the intermediate ε-$Li_{0.5}V_2O_5$. The second Li-ion intercalation occurred in the range of 2.1 to 2.5 V vs Li/Li^+, corresponding to the irreversible formation of y-$Li_2V_2O_5$ [5, 50].

Figure 4: Cyclic voltammograms over 2 cycles at 0.1 mV s^{-1} for (a) V_2O_5 with ΔE_P labelled for the α/ε, ε/δ, and δ/γ transitions, (b) 2%Na^+-V_2O_5, (c) 3%Ba^{2+}-V_2O_5 and (d) 3%Al^{3+}-V_2O_5.

The first phase change in the range of 3.0 to 3.5 V vs Li/Li^+ (α/ε and ε/δ) appeared to be of similar shape for all tested materials, implying that the structural variations occurring during this phase change were similar. Redox peak separations (ΔE_p) for the α/ε, ε/δ, and δ/γ transitions were calculated for each sample. The smallest peak separations were 0.15, 0.24 and 0.24 V for 3%Ba^{2+}-V_2O_5, whilst the largest separations at 0.31, 0.40, and 0.53 V corresponded to 3%Al^{3+}-V_2O_5. Additionally, the CV for 3%Ba^{2+}-V_2O_5 possessed quite sharp peaks, especially the delithiation peak at 2.6 V vs Li/Li^+, indicating improved ionic diffusion. Peak separations for undoped V_2O_5 and 2%Na^+-V_2O_5 were similar at 0.24, 0.33 and 0.46 V and 0.24, 0.32 and 0.41 V, for the α/ε, ε/δ, and δ/γ transitions. This suggested that polarisation decreased and reversibility increased for the 3%Ba^{2+}-V_2O_5 and 2%Na^+-V_2O_5 samples [51]. Additionally, the small shoulder peaks in the range 3.5 to 3.7 V vs Li/Li^+ for undoped V_2O_5, 2%Na^+-V_2O_5 and 3%Ba^{2+}-V_2O_5, indicated the availability of multiple active Li-ion sites for multi-stepped

lithiation/delithiation [52]. Two minor cathodic peaks in 2.3 to 2.4 V vs Li/Li^+ are observed for undoped V_2O_5 and 3% Ba^{2+}-V_2O_5, also attributed to multiple Li-ion site, are absent in 2%Na^+-V_2O_5 suggesting a small variation in the charge transfer processes for this material. The extra redox peaks in the CV for 2%Na^+-V_2O_5 at *ca*. 2.85 V vs Li/Li^+ (lithiation) and 2.98 V vs Li/Li^+ (delithiation), has been previously attributed to the presence of electrochemically active vanadium oxides with significant amounts of lower oxidation state V^{4+} [39, 53]. This observation does not seem to be relevant herein given that a comparable V^{4+} content was determined for V_2O_5, 2%Na^+-V_2O_5 and 3%Ba^{2+}-V_2O_5 at 8, 11 and 9%, respectively. These peaks were also previously observed in the CV of Na-preinserted V_2O_5 by Li *et al.*, although no suggestions were given to their assignment [31]. As there is a significant proportion of NaV_6O_{15} impurity present (6 at%) in 2%Na^+-V_2O_5, it is more likely that these extra redox peaks were the result of Li-ion interaction with this phase rather than the V^{4+} content. This will be discussed in more detail later. There are also strong shoulder peaks associated with the δ/γ transition for 2%Na^+-V_2O_5 at *ca*. 2.45 V vs Li/Li^+ (lithiation) and *ca*. 2.78 V vs Li/Li^+ (delithiation). Liu *et al.* attributed lithiation peaks in a similar region in their CV for NaV_6O_{15} to a multistep Li-ion insertion process through its tunnel-like structure which are formed *via* $(V_2O_5)_x$ chains with Na^+ orientated along the *b* axis [24].

Capacity versus potential profiles for the materials cycled at 50 mA g^{-1} are shown in Figure 5(a,b) for the 1st and 5th cycles, respectively. The potential plateaus at *ca.* 2.2 V vs Li/Li^+ and at > 3.1 V vs Li/Li^+, predictably correspond to the phase transitions of ε-$Li_{0.5}V_2O_5$, δ-LiV_2O_5, and γ-$Li_2V_2O_5$, which match well with the redox peaks in Figure 4.

Figure 5: Capacity vs potential profiles of V_2O_5, 2%Na^+-V_2O_5, 3%Ba^{2+}-V_2O_5 and 3%Al^{3+}- V_2O_5 at 50 mA g^{-1} for (a) cycle 1 and (b) cycle 5 from the C-rate test, (c) C-rate test at the following current densities: 50 mA g^{-1}, 100 mA g^{-1}, 300 mA g^{-1}, and 600 mA g^{-1} for 10 cycles each with cycling over 50 cycles at 50 mA g^{-1} following the C-rate test.

The extra redox peaks for 2%Na^+-V_2O_5 observed in the CV in Figure 4(b) are clearly observed in Figure 5(a) as potential plateaus located at *ca*. 2.85 V vs Li/Li^+ (lithiation) and *ca*. 3.0 V vs Li/Li^+ (delithiation). The potential plateaus at *ca*. 2.48 V vs Li/Li^+ (lithiation) and *ca*. 2.72 V vs Li/Li^+ (delithiation) match the strong shoulder redox peaks from Figure 4(b). These extra potential plateaus have been previously observed in lithiation capacity versus potential profiles for NaV_6O_{15} nanorods [24]. They were attributed to the formation of $LiNaV_6O_{15}$ in the range of 2.85 to 3.5 V vs Li/Li^+ and $Li_2NaV_6O_{15}$ within the range of 2.5 to 2.8 V vs Li/Li^+. Similarly placed redox peaks and potential plateaus were also attributed to the removal of Na^+ from the host material in NaV_6O_{15} by Hu *et al.*, allowing more Li-ions to be inserted

forming a lithiated NaV_6O_{15} phase, thus maintaining high capacities with subsequent cycling [54]. These extra redox peaks and potential plateaus were also observed by Zhu *et al.* [53] and Mai *et al.* [39], which were attributed to other active vanadium oxides of lower valences according to a review on layered vanadium oxides by Chernova *et al.* [55]. The 3%Ba^{2+}-V_2O_5 possesses a similar V^{4+} content (9%) as 2%Na^+-V_2O_5 (11%) and V_2O_5 (8%) though no potential plateaus at *ca*. 2.9 V vs Li/Li^+ and *ca*. 2.5 V vs Li/Li^+ are observed. This leads to the conclusion that the V^{4+} content was not responsible for these extra redox peaks [Figure 4(b)] and potential plateaus [Figure 5(b)] as it is more likely that the NaV_6O_{15} impurity or extraction of Na^+ from the 2%Na^+-doped V_2O_5 phase was the reason.

The irreversible capacity losses (ICL) from cycle 1 in Figure 5(a) are representative of charge storage across a Li-ion layer build up. According to Table 2(a), ICLs for V_2O_5, 2%Na^+-V_2O_5, 3%Ba^{2+}-$V_2O_5$and 3%Al^{3+}-V_2O_5 were 23.2, 49.6, 19.4 and 1.4 mAh g^{-1}, respectively. For the materials tested herein, no correlation between irreversible capacity loss and surface area was observed. Further discussion about these ICL values is provided in Supplementary Section 3.

The results of a C-rate test at 50, 100, 300, and then 600 mA g^{-1} (over 10 cycles at each current density) immediately followed by a cycling test at 50 mA g^{-1} (for a further 50 cycles) is presented in Figure 5(c). Cycle stability was generally improved for the doped materials which is clear in the first 10 cycles at 50 mA g^{-1} [Figure 5(c)] with capacities and stabilities of 226 mAh g^{-1} (n = 2) and 81% for V_2O_5, 230 mAh g^{-1} (n = 2) and 85% for 2%Na^+-V_2O_5, 268 mAh g^{-1} (n = 2) and 90% for 3%Ba^{2+}-V_2O_5, and 138 mAh g^{-1} (n = 2) and 94% for 3%Al^{3+}-V_2O_5. The increased cycle stability at higher currents was visibly observable in the C-rate data and was due to a decrease in side reactions within the cells [56]. The capacity retention data with varying current densities is summarised in Table 2(b), showing improvements for the doped materials compared to the undoped sample, especially for 3%Ba^{2+}-V_2O_5. Both undoped V_2O_5 and 3%Al^{3+}-V_2O_5 had negligible capacities at 600 mA g^{-1}, whilst rate retention noticeably improved for 2%Na^+-V_2O_5 and 3%Ba^{2+}-V_2O_5. Despite the poor performance at 600 mA g^{-1}, all materials recovered well when the cycling current rate was returned to 50 mA g^{-1}. The Coulombic efficiencies for the C-rate tests in Figure S3 were much more impressive for 2%Na^+-V_2O_5 and 3%Ba^{2+}-V_2O_5 compared to the undoped V_2O_5 and 3%Al^{3+}-V_2O_5 samples (especially at 300 mA g^{-1}). Coulombic

efficiencies were particularly erratic for undoped V_2O_5 and 3%Al^{3+}-V_2O_5 at 600 mA g^{-1} due to the extremely small capacities obtained at this current density (thus, data not included).

When considering the effect of surface area on rate capability, undoped V_2O_5 possessed both the lowest surface area (8.7 m^2 g^{-1}) and lowest rate capabilities. Interestingly, 3%Al^{3+}-V_2O_5, despite having the largest surface area of the materials examined herein (22.2 m^2 g^{-1}), did not result in substantial rate capability improvement. This suggests that the surface area is not the only significant factor in rate capability improvement for these materials and that aspects such as dopant type/location or conductivity variations, are also important [32, 57, 58]. The capacity, capacity retention and Coulombic efficiencies (Figure S3) for the 60 cycles at 50 mA g^{-1} following the C-rate test is summarised in Table 2(c). The efficiencies of 2%Na^+-V_2O_5 and 3%Ba^{2+}-V_2O_5 were lower than that of undoped V_2O_5 and 3%Al^{3+}-V_2O_5which contrasts with the rate capability performances. Interestingly, Table 2(c) shows that the effect of a dopant on long term cycling is minor with minimal cycle retention improvements for 2%Na^+-V_2O_5 and 3%Ba^{2+}-V_2O_5 compared to undoped V_2O_5. This shows that degradation issue with long term cycling remains unsolved suggesting another cause such as structural variations in the V_2O_5 crystal or electrolyte degradation.

Table 2: Cycling data (a) for irreversible capacity loss for n = 1, (b) capacities at n = 5, 15, 25, 35 at each current density, (c) cycling stability after C-rate at 50 mA g^{-1} (42 < n < 100).

	a	b				c		
Sample	ICL (mAh g^{-1})	n = 5 at 50 mA g^{-1}	n = 15 at 100 mA g^{-1}	n = 25 at 300 mA g^{-1}	n = 35 at 600 mA g^{-1}	n = 42 (mAh g^{-1})	Capacity retention (%)	Coulombic efficiencies (%)
V_2O_5	23.2	204	141	3	N/A	166	80	98
2%Na^+-V_2O_5	49.6	210	182	110	14	182	82	97
3%Ba^{2+}-V_2O_5	19.4	260	218	170	120	216	83	98
3%Al^{3+}-V_2O_5	1.4	135	104	15	N/A	124	74	97

Impedance measurements were undertaken to compare the relative conductivities of the electrospun materials with resultant Nyquist plots in Figure 6. All Nyquist plots are composed of a distorted

depressed semicircle in the high-to-moderate frequency range and a small upturning in the low frequency range.

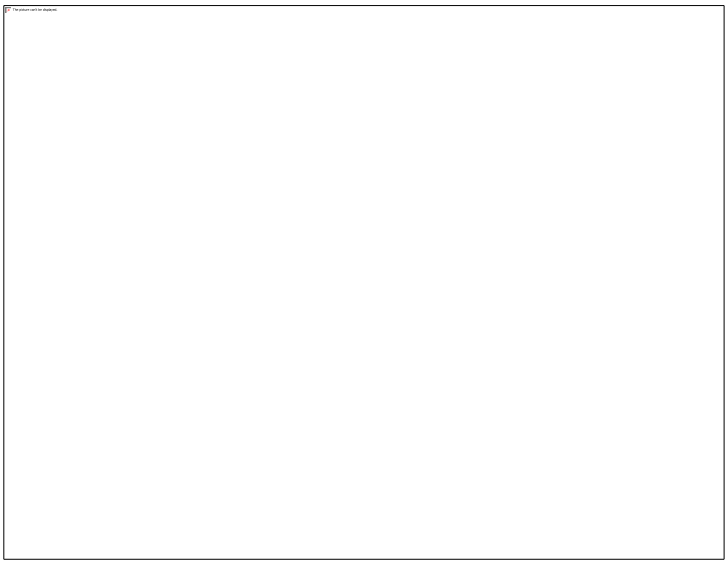

Figure 6: Nyquist plots of pristine cells consisting of a distorted semicircle and small up turning.

The diameter of the depressed semicircle is representative of the charge transfer resistance, R_{ct}. A decrease in R_{ct} represents higher intrinsic conductivity resulting in improved electrochemical performance [30, 32, 59]. 2%Na^{+}-V_2O_5 and 3%Ba^{2+}-V_2O_5 possess smaller R_{ct} compared to V_2O_5 which is reflected in the proceeding electrochemical analysis. Conversely, the large semicircular trace in the Nyquist plot for 3Al^{3+}-V_2O_5 suggesting low intrinsic conductivity supports the observed electrochemical performance in Figure 4 and Figure 5. A detailed discussion of the impedance results can be found in Supplementary Section 4.

3. Atomistic simulations

To rationalise the conductivity and electrochemical performance incurred by the different dopants, their locations in the V_2O_5 structure were investigated using atomistic simulations. Dopants can be incorporated either substitutionally or interstitially into V_2O_5, with different charge compensating effects as a result. Substitutional replacement of V^{5+} by the relevant cations can be compensated by the formation of oxygen vacancies, which in Kroger-Vink notation is expressed as:

$$\frac{1}{2}Al_2O_3 + VO_{VO}^{X} \leftrightarrows Al_{VO}^{X} + \frac{1}{2}V_2O_5 \quad (1)$$

$$BaO + VO_{VO}^{X} + \frac{1}{2}O_{O}^{X} \leftrightarrows Ba'_{VO} + \frac{1}{2}\square_{O}^{\bullet\bullet} + \frac{1}{2}V_2O_5 \quad (2)$$

$$\frac{1}{2}Na_2O + VO_{VO}^{X} + O_{O}^{X} \leftrightarrows Na''_{VO} + \square_{O}^{\bullet\bullet} + \frac{1}{2}V_2O_5 \quad (3)$$

Where VO_{VO}^{X} indicates a $(V\text{-}O)^{3+}$ vanadyl group in the V_2O_5 lattice, Al_{VO}^{X} indicates an Al^{3+} ion replacing a V-O vanadyl group with neutral overall charge, and $\square_{O}^{\bullet\bullet}$ indicates an oxygen-ion vacancy with a net positive charge of +2. The simultaneous 'clustered' replacement of a V-O vanadyl group (i.e. the V and the O with shortest V-O bond distance) by the dopants has a lower formation energy than isolated $M_V + \square_{O}^{\bullet\bullet}$ defects and is therefore considered as the main scheme for forming oxygen vacancies due to substitutional doping. Interstitial incorporation of the cations can be accompanied by either oxide interstitials:

$$\frac{1}{2}Al_2O_3 \leftrightarrows Al_{i}^{\bullet\bullet\bullet} + \frac{3}{2}O_{i}'' \quad (4)$$

$$BaO \leftrightarrows Ba_{i}^{\bullet\bullet} + O_{i}'' \quad (5)$$

$$\frac{1}{2}Na_2O \leftrightarrows Na_{i}^{\bullet} + \frac{1}{2}O_{i}'' \quad (6)$$

or vanadium vacancies:

$$\frac{1}{2}Al_2O_3 \leftrightarrows Al_{i}^{\bullet\bullet\bullet} + \frac{3}{5}\square_{V}''''' + \frac{3}{10}V_2O_5 \quad (7)$$

$$BaO \leftrightarrows Ba_{i}^{\bullet\bullet} + \frac{2}{5}\square_{V}''''' + \frac{1}{5}V_2O_5 \quad (8)$$

$$\frac{1}{2}Na_2O \leftrightarrows Na_{i}^{\bullet} + \frac{1}{5}\square_{V}''''' + \frac{1}{10}V_2O_5 \quad (9)$$

Where $Al_{i}^{\bullet\bullet\bullet}$ represents Al^{3+}, $Ba_{i}^{\bullet\bullet}$ is Ba^{2+}, $Na_{i}^{\bullet}$ is Na^{+} and $\square_{V}'''''$ are vanadium vacancies.

The calculated defect formation energies are reported in Table 4. The interstitial cation defects compensated by vanadium vacancies have high formation energies and are thus unlikely to occur. The Al^{3+} substitutional defect is lower in energy than the interstitial defect by 2 eV, and we can therefore

infer that under thermodynamic control Al^{3+} will predominantly occupy substitutional sites. However, the relatively small energy difference between substitutional and interstitial sites means that it may be possible for Al^{3+} to occupy interstitial sites under some conditions. For Ba^{2+} and Na^{+}, the interstitial cation defects with oxygen interstitials are significantly lower in energy than the substitutional sites by 8.6 and 14.4 eV, respectively. Due to the greater energy difference between the substitutional and interstitial sites, our calculations indicate that these cations will only occupy interstitial sites.

Table 4: Calculated defect formation energies for substitutional and interstitial defect sites.

Defect site	Charge compensation	Species	Defect energy / eV	Equation
Substitutional	Oxygen vacancies	Al^{3+}	0.66	1
		Ba^{2+}	5.61	2
		Na^{+}	9.80	3
Interstitial	Oxide interstitial	Al^{3+}	2.64	4
		Ba^{2+}	-2.96	5
		Na^{+}	-4.58	6
	Vanadium vacancy	Al^{3+}	23.57	7
		Ba^{2+}	11.26	8
		Na^{+}	2.84	9

Undoped V_2O_5 is oxygen deficient and shows intrinsic n-type semiconducting behaviour, displaying a measurable concentration of oxygen vacancies, charge balanced by V^{4+} ions. Writing the formation of intrinsic defects in Kroger-Vink notation:

$$V_V^X + O_O^X \leftrightarrows 2V_V' + \square_O^{\bullet\bullet} + \frac{1}{2}O_2 \qquad (10)$$

The chemical equilibrium linking the concentration of O vacancies and the partial reduction of V^{5+} (d^0) to V^{4+} (d^1), which keeps the bulk material electronically neutral will be governed by an equilibrium constant expressed by the mass law:

$$K_{int} = [\square_O^{\bullet\bullet}][V_V']^2 \cdot pO_2^{\frac{1}{2}} \quad (11)$$

For intrinsic defects in undoped V_2O_5 the concentration of oxygen vacancies $[\square_O^{\bullet\bullet}]$ is approximately equivalent to half the concentration of V^{4+} ($[V_V']$):

$$[\square_O^{\bullet\bullet}] \approx \frac{1}{2}[V_V'] \quad (12)$$

The introduction of interstitial Ba^{2+} or Na^+ is accompanied by increased O content. In stoichiometric V_2O_5 this generates interstitial O ions, while in n-type V_2O_5 the additional oxygen will anneal out some of the intrinsic O vacancies. The equation expressing the link between intrinsic defects and dopant concentration becomes:

$$2\,[\square_O^{\bullet\bullet}] + [Na_i^{\bullet}] \approx [V_V'] \quad (13)$$

and modifies the equilibrium concentrations. Doping with interstitial dopants (such as Na^+ and Ba^{2+}) therefore lowers the concentration of oxygen vacancies, whilst increasing the concentration of V^{4+}. This result explains the increased V^{4+} concentrations in the Na^+ and Ba^{2+} doped samples compared to undoped V_2O_5 observed in our XPS measurements.

The introduction of substitutional Al^{3+} ions is instead accompanied by creation of oxygen vacancies, and the expression linking the concentration of Al^{3+} and intrinsic defects is now:

$$[\square_O^{\bullet\bullet}] = \frac{1}{2}[V_V'] + [Al_V''] \quad (16)$$

The presence of oxygen vacancies associated with the Al^{3+} dopant therefore makes the creation of further vacancies through reduction of V more difficult, resulting in an Al^{3+}-doped V_2O_5 material with lower V^{4+} content than undoped V_2O_5. The large overpotentials [Figure 5(a,b)] suggested fewer nucleation centres for phase transitions during lithiation/delithiation [60], which in the light of results discussed above may correspond to intrinsic oxygen vacancies (i.e those not associated with the Al dopants).

4. Overall Discussion

The presence of V^{4+} in undoped V_2O_5 indicated an intrinsic n-type semiconducting nature, where an equilibrium was created between oxygen vacancies and reduced vanadium ions. The reduction of V^{5+} (d^0) to V^{4+} (d^1) has previously been linked to improved electronic conductivity, as the d^1 electrons can 'hop' between vanadium sites [25]. The incorporation of the dopants had a clear effect on the ratio of V^{4+}:V^{5+} and likely modified the oxygen vacancy concentration.

The electronic conductivity of doped V_2O_5, linked with the concentration of V^{4+}, increased upon doping with Ba^{2+} and Na^+. Li *et al.* suggested that the introduction of Na^+ caused the reduction of V^{5+} rather than the substitution of vanadium [31]. With the presence of 6 at% of NaV_6O_{15} impurity, as determined by Rietveld refinement, the extra redox peaks and potential plateaus observed in Figure 4 and Figure 5, respectively, was caused by partial substitution of Na^+ for Li-ions with this impurity phase [24]. The NaV_6O_{15} impurity may also have contributed to the improved capacity of 2%Na^+-V_2O_5 given its tunnel-like structure.

The predictions from Equation 16, regarding oxygen vacancy creation, correlated with the observed reduction in V^{4+} concentration for the Al^{3+} doped material (2%) with respect to the undoped V_2O_5 (8%) in the XPS analysis. The reduction in V^{4+} concentration played a significant role in decreasing the electronic conductivity and Li-ion transport and thus limiting the electrochemical performance for 3%Al^{3+}-V_2O_5. Experimentally, this was observed with low capacities in the C-rate test, large redox peak separations in the CV and in the impedance results with a decreased R_{ct} implying increased oxygen vacancies [28,29].

Al^{3+} doped materials have received positive attention in the literature, although 3%Al^{3+}-V_2O_5 reported herein did not perform to the expectations presented by others [21, 22, 61]. Zhan *et al.* used a soft-chemical method with V_2O_5 powder and aluminium nitrate assisted by oxalic acid followed by heat treatment at 350 °C to obtain V_2O_5 nanoparticles with 9 at% loading of Al^{3+} [21]. Zhu *et al.* also used a soft chemical method with the same components and reduced graphene oxide to produce V_2O_5 and V_2O_5 incorporated reduce graphene oxide both with 7 at% loadings of Al^{3+} [61]. Cheah *et al.*

electrospun 20 and 33 at% Al^{3+} doped V_2O_5 fibres from a solution of vanadyl acetylacetonate, aluminium nitrate and poly(vinylpyrrolidone) followed by heat treatment at 400 °C [22]. Finally, all studies showed an increased in V^{4+} for the Al^{3+} doped V_2O_5 *via* XPS measurements.

It is likely then the combination of different starting materials, higher heat treatment temperature (nucleation variations) and lower Al^{3+} loading used herein, is responsible for the substitutional Al^{3+} dopant location and low V^{4+} content, which resulted in relatively poor performance in this material. The energetics of Al^{3+} incorporation suggested that substitutional sites are favoured, but interstitial sites may be accessible under some conditions. Whilst Cheah *et al.* also used electrospinning, the higher loading (20 and 33 at%) may tend to favour interstitial Al^{3+} sites, or a mixture of substitutional and interstitial doping. Despite these high dopant loadings, no impurity reflections were observed in their XRD results. These variations in synthesis methods clearly indicate the important role that starting materials and fabrication method play on the resultant V^{4+} content.

The results presented herein show that the interstitial Na^{+} and Ba^{2+} dopants in electrospun V_2O_5 provided both improved structural and enhanced electronic effects for the V_2O_5 structure and result in improved electrochemical performance. In contrast, Al^{3+} doping in this work provided improved structural stability but decreased electronic conductivity. Furthermore, the results showed that the investigated dopants produced multiple effects in terms of their location, loading and oxidation state, on both the stabilization of the host structure and on electronic conductivity. Given this series of variables, a general conclusion about valence state alone cannot be provided. The analysis in this project suggests that dopants with low valence state are electronically and structurally favourable, however, dopant loading must also be considered. Thus, dopant type, concentration and oxidation state are critical in determining the mode of incorporation of the dopant, which in turn affects the overall electrochemical performance of the host material through control of intrinsic defects.

4. **Conclusions**

Electrospinning was used to produce microscale fibres consisting of nanostructured particles made up of doped V_2O_5. Na^+, Ba^{2+}, Al^{3+} were systematically incorporated into V_2O_5 to produce 2%Na^+-V_2O_5, 3%Ba^{2+}-V_2O_5, and 3%Al^{3+}-V_2O_5, respectively. Ba^{2+} was investigated to determine whether the dopant loading was responsible for the reduced capacity compared to the undoped material. All dopants offered improved rate capability but only 2%Na^+-V_2O_5 and 3%Ba^{2+}-V_2O_5 showed improved cycle stability and improved capacities indicating an increase in structural stability, afforded by the dopants, and an increase in electrical conductivity is necessary for overall enhanced electrochemical performance. Another key parameter that dictated the performance of these materials was the V^{4+} content where 3%Al^{3+}-V_2O_5 possessed the lowest V^{4+} concentration along with the poorest electrochemical performance. The location of the dopants, V^{4+} content and electronic conductivity were rationalised by atomistic simulations, from which we can infer that interstitial dopants are important to improved electrochemical performance. After examination of the literature, we suggest that synthesis methods of nanomaterials require careful consideration to optimise oxidation state concentrations.

References

1. Cavaliere S, Subianto S, Savych I, Jones DJ, Roziere J (2011) Electrospinning: designed architectures for energy conversion and storage devices. Energy Environ Sci 4:4761–4785 . doi: 10.1039/C1EE02201F

2. McNulty D, Buckley DN, O'Dwyer C (2014) Synthesis and electrochemical properties of vanadium oxide materials and structures as Li-ion battery positive electrodes. J Power Sources 267:831–873 . doi: 10.1016/j.jpowsour.2014.05.115

3. Whittingham MS (1976) The Role of Ternary Phases in Cathode Reactions. J Electrochem Soc 123:315–320

4. Yu JJ, Yang J, Nie WB, Li ZH, Liu EH, Lei GT, Xiao QZ (2013) A porous vanadium pentoxide nanomaterial as cathode material for rechargeable lithium batteries. Electrochimica Acta 89:292–299 . doi: 10.1016/j.electacta.2012.11.032

5. Pan A, Zhang J-G, Nie Z, Cao G, Arey BW, Li G, Liang S, Liu J (2010) Facile synthesized nanorod structured vanadium pentoxide for high-rate lithium batteries. J Mater Chem 20:9193 . doi: 10.1039/c0jm01306d

6. Mai L, An Q, Wei Q, Fei J, Zhang P, Xu X, Zhao Y, Yan M, Wen W, Xu L (2014) Nanoflakes-Assembled Three-Dimensional Hollow-Porous V_2O_5 as Lithium Storage Cathodes with High-Rate Capacity. Small 10:3032–3037 . doi: 10.1002/smll.201302991

7. Surnev S, Ramsey M., Netzer F. (2003) Vanadium oxide surface studies. Prog Surf Sci 73:117–165 . doi: 10.1016/j.progsurf.2003.09.001

8. Armer CF, Yeoh JS, Li X, Lowe A (2018) Electrospun vanadium-based oxides as electrode materials. J Power Sources 395:414–429 . doi: 10.1016/j.jpowsour.2018.05.076

9. Giorgetti M, Passerini S, Smyrl WH, Berrettoni M (2000) Evidence of Bilayer Structure in V2O5 Xerogel. Inorg Chem 39:1514–1517 . doi: 10.1021/ic9913233

10. Moretti A, Passerini S (2016) Bilayered Nanostructured V2O5·nH2O for Metal Batteries. Adv Energy Mater 6:1600868-n/a . doi: 10.1002/aenm.201600868

11. Sakunthala A, Reddy MV, Selvasekarapandian S, Chowdari BVR, Selvin PC (2011) Energy storage studies of bare and doped vanadium pentoxide, (V1.95M0.05)O5, M = Nb, Ta, for lithium ion batteries. Energy Environ Sci 4:1712–1725 . doi: 10.1039/C0EE00513D

12. Delmas C, Cognac-Auradou H, Cocciantelli JM, Ménétrier M, Doumerc JP (1994) The LixV2O5 system: An overview of the structure modifications induced by the lithium intercalation. Solid State Ion 69:257–264 . doi: 10.1016/0167-2738(94)90414-6

13. Yan L. Cheah, Aravindan V, Srinivasan Madhavi (2013) Chemical Lithiation Studies on Combustion Synthesized V2O5 Cathodes with Full Cell Application for Lithium Ion Batteries. J Electrochem Soc 160:A1016–A1024 . doi: 10.1149/2.015308jes

14. Winter M, Besenhard JO, Spahr ME, Novak P (1998) Insertion Electrode Materials for Rechargeable Lithium Batteries. Adv Mater 10:725–763

15. Liang S, Qin M, Tang Y, Zhang Q, Li X, Tan X, Pan A (2014) Facile synthesis of nanosheet-structured V2O5 with enhanced electrochemical performance for high energy lithium-ion batteries. Met Mater Int 20:983–988 . doi: 10.1007/s12540-014-5025-7

16. Takahashi K, Wang Y, Lee K, Cao G (2006) Fabrication and Li+-intercalation properties of V2O5-TiO2 composite nanorod arrays. Appl Phys A 82:27–31 . doi: 10.1007/s00339-005-3375-1

17. Chen CH, Liu J, Stoll ME, Henriksen G, Vissers DR, Amine K (2004) Aluminum-doped lithium nickel cobalt oxide electrodes for high-power lithium-ion batteries. J Power Sources 128:278–285 . doi: 10.1016/j.jpowsour.2003.10.009

18. Johnson ID, Blagovidova E, Dingwall PA, Brett DJL, Shearing PR, Darr JA (2016) High power Nb-doped LiFePO4 Li-ion battery cathodes; pilot-scale synthesis and electrochemical properties. J Power Sources 326:476–481 . doi: 10.1016/j.jpowsour.2016.06.128

19. Chung S-Y, Bloking JT, Chiang Y-M (2002) Electronically conductive phospho-olivines as lithium storage electrodes. Nat Mater 1:123–128 . doi: 10.1038/nmat732

20. Wu Y, Zhu P, Zhao X, Reddy MV, Peng S, Chowdari BVR, Ramakrishna S (2013) Highly improved rechargeable stability for lithium/silver vanadium oxide battery induced viaelectrospinning technique. J Mater Chem A 1:852–859 . doi: 10.1039/C2TA00042C

21. Zhan S, Wei Y, Bie X, Wang C, Du F, Chen G, Hu F (2010) Structural and electrochemical properties of Al3+ doped V2O5 nanoparticles prepared by an oxalic acid assisted soft-chemical method. J Alloys Compd 502:92–96 . doi: 10.1016/j.jallcom.2010.03.133

22. Cheah YL, Aravindan V, Madhavi S (2012) Improved Elevated Temperature Performance of Al-Intercalated V2O5 Electrospun Nanofibers for Lithium-Ion Batteries. ACS Appl Mater Interfaces 4:3270–3277 . doi: 10.1021/am300616k

23. Armer CF, Lübke M, Reddy MV, Darr JA, Li X, Lowe A (2017) Phase change effect on the structural and electrochemical behaviour of pure and doped vanadium pentoxide as positive electrodes for lithium ion batteries. J Power Sources 353:40–50 . doi: 10.1016/j.jpowsour.2017.03.121

24. Liu H, Wang Y, Li L, Wang K, Hosono E, Zhou H (2009) Facile synthesis of NaV6O15 nanorods and its electrochemical behavior as cathode material in rechargeable lithium batteries. J Mater Chem 19:7885 . doi: 10.1039/b912906e

25. Coustier F, Passerini S, Smyrl WH (1997) Dip-coated silver-doped V2O5 xerogels as host materials for lithium intercalation. Solid State Ion 100:247–258 . doi: 10.1016/S0167-2738(97)00354-8

26. Coustier F, Hill J, Owens BB, Passerini S, Smyrl WH (1999) Doped vanadium oxides as host materials for lithium intercalation. J Electrochem Soc 146:1355–1360

27. Zhan S, Chen G, Liu D, Li A, Wang C, Wei Y (2009) Effects of Cr doping on the structural and electrochemical properties of V2O5. J Alloys Compd 479:652–656 . doi: 10.1016/j.jallcom.2009.01.023

28. Wei Y, Ryu C-W, Kim K-B (2007) Improvement in electrochemical performance of V2O5 by Cu doping. J Power Sources 165:386–392 . doi: 10.1016/j.jpowsour.2006.12.016

29. Venkatesan A, Krishna Chandar NR, Kandasamy A, Karl Chinnu M, Marimuthu KN, Mohan Kumar R, Jayavel R (2015) Luminescence and electrochemical properties of rare earth (Gd, Nd) doped V2O5 nanostructures synthesized by a non-aqueous sol-gel route. RSC Adv 5:21778–21785 . doi: 10.1039/C4RA14542A

30. Liang X, Gao G, Liu Y, Zhang T, Wu G (2017) Synthesis and characterization of Fe-doped vanadium oxide nanorods and their electrochemical performance. J Alloys Compd 715:374–383 . doi: 10.1016/j.jallcom.2017.04.242

31. Li X, Liu C, Zhang C, Fu H, Nan X, Ma W, Li Z, Wang K, Wu H, Cao G (2016) Effects of Preinserted Na Ions on Li-Ion Electrochemical Intercalation Properties of V2O5. ACS Appl Mater Interfaces 8:24629–24637 . doi: 10.1021/acsami.6b08052

32. Li Z, Zhang C, Liu C, Fu H, Nan X, Wang K, Li X, Ma W, Lu X, Cao G (2016) Enhanced Electrochemical Properties of Sn-doped V2O5 as a Cathode Material for Lithium Ion Batteries. Electrochimica Acta 222:1831–1838 . doi: 10.1016/j.electacta.2016.11.174

33. Zeng H, Liu D, Zhang Y, See KA, Jun Y-S, Wu G, Gerbec JA, Ji X, Stucky GD (2015) Nanostructured Mn-Doped V2O5 Cathode Material Fabricated from Layered Vanadium Jarosite. Chem Mater 27:7331–7336 . doi: 10.1021/acs.chemmater.5b02840

34. Giorgetti M, Berrettoni M, Smyrl WH (2007) Doped V2O5-Based Cathode Materials: Where Does the Doping Metal Go? An X-ray Absorption Spectroscopy Study. Chem Mater 19:5991–6000 . doi: 10.1021/cm701910c

35. Tepavcevic S, Xiong H, Stamenkovic VR, Zuo X, Balasubramanian M, Prakapenka VB, Johnson CS, Rajh T (2012) Nanostructured Bilayered Vanadium Oxide Electrodes for Rechargeable Sodium-Ion Batteries. ACS Nano 6:530–538 . doi: 10.1021/nn203869a

36. Pham-Cong D, Ahn K, Hong SW, Jeong SY, Choi JH, Doh CH, Jin JS, Jeong ED, Cho CR (2014) Cathodic performance of V2O5 nanowires and reduced graphene oxide composites for lithium ion batteries. Curr Appl Phys 14:215–221 . doi: 10.1016/j.cap.2013.10.022

37. Cheah YL, Gupta N, Pramana SS, Aravindan V, Wee G, Srinivasan M (2011) Morphology, structure and electrochemical properties of single phase electrospun vanadium pentoxide nanofibers for lithium ion batteries. J Power Sources 196:6465–6472 . doi: 10.1016/j.jpowsour.2011.03.039

38. Wang H, Ma D, Huang Y, Zhang X (2012) Electrospun V2O5 Nanostructures with Controllable Morphology as High-Performance Cathode Materials for Lithium-Ion Batteries. Chem - Eur J 18:8987–8993 . doi: 10.1002/chem.201200434

39. Mai L, Xu L, Han C, Xu X, Luo Y, Zhao S, Zhao Y (2010) Electrospun Ultralong Hierarchical Vanadium Oxide Nanowires with High Performance for Lithium Ion Batteries. Nano Lett 10:4750–4755 . doi: 10.1021/nl103343w

40. Cheah YL, Aravindan V, Madhavi S (2013) Synthesis and Enhanced Lithium Storage Properties of Electrospun V2O5 Nanofibers in Full-Cell Assembly with a Spinel Li4Ti5O12 Anode. ACS Appl Mater Interfaces 5:3475–3480 . doi: 10.1021/am400666n

41. Lutterotti L, Matthies S, Wenk H (1999) MAUD (Material Analysis Using Diffraction): a user friendly Java program for Rietveld Texture Analysis and more. Twelfth Int Conf Textures Mater ICOTOM-12 1599:

42. Islam MS, Fisher CAJ (2014) Lithium and sodium battery cathode materials: computational insights into voltage, diffusion and nanostructural properties. Chem Soc Rev 43:185–204 . doi: 10.1039/C3CS60199D

43. Catlow CRA (1997) Computer Modelling in Inorganic Crystallography. Academic Press, San Diego

44. Gale JD, Rohl AL (2003) The General Utility Lattice Program (GULP). Mol Simul 29:291–341 . doi: 10.1080/0892702031000104887

45. Shklover V, Haibach T, Nespar R, Novak P, Reid F (1996) Crystal structure of the produce of Mg2+ insertion into V2O5 single crystals Locality: synthetic Sample:IIb. J Solid State Chem 123:317–323

46. Sun D, Jin G, Wang H, Liu P, Ren Y, Jiang Y, Tang Y, Huang X (2014) Aqueous rechargeable lithium batteries using NaV6O15 nanoflakes as high performance anodes. J Mater Chem A 2:12999–13005 . doi: 10.1039/C4TA01675K

47. Liu J, Guo W, Qu F, Feng C, Li C, Zhu L, Zhou J, Ruan S, Chen W (2014) V-doped In2O3 nanofibers for H2S detection at low temperature. Ceram Int 40:6685–6689 . doi: 10.1016/j.ceramint.2013.11.129

48. Nayak S, Sahoo B, Chaki TK, Khastgir D (2014) Facile preparation of uniform barium titanate ($BaTiO_3$) multipods with high permittivity: impedance and temperature dependent dielectric behavior. RSC Adv 4:1212–1224 . doi: 10.1039/C3RA44815K

49. Marsh J, Minel L, Barthes-Labrousee MG, Gorse D (1998) Interaction of epoxy model molecules with aluminium, anodised titanium and copper surfaces: an XPS study. Appl Surf Sci 133:270–286

50. Zhao H, Pan L, Xing S, Luo J, Xu J (2013) Vanadium oxides–reduced graphene oxide composite for lithium-ion batteries and supercapacitors with improved electrochemical performance. J Power Sources 222:21–31 . doi: 10.1016/j.jpowsour.2012.08.036

51. Qin M, Liu J, Liang S, Zhang Q, Li X, Liu Y, Lin M (2014) Facile synthesis of multiwalled carbon nanotube–V2O5 nanocomposites as cathode materials for Li-ion batteries. J Solid State Electrochem 18:2841–2846 . doi: 10.1007/s10008-014-2543-7

52. Kawakita J, Majima M, Miura T, Kishi T (1997) Preparation and lithium insertion behaviour of oxygen-deficient Li1 + xV3O8 − δ. J Power Sources 66:135–139 . doi: 10.1016/S0378-7753(96)02540-2

53. Zhu C, Shu J, Wu X, Li P, Li X Electrospun V2O5 micro/nanorods as cathode materials for lithium ion battery. J Electroanal Chem. doi: 10.1016/j.jelechem.2015.11.013

54. Hu F, Jiang W, Dong Y, Lai X, Xiao L, Wu X (2017) Synthesis and electrochemical performance of NaV6O15 microflowers for lithium and sodium ion batteries. RSC Adv 7:29481–29488 . doi: 10.1039/C7RA04388K

55. Chernova NA, Roppolo M, Dillon AC, Whittingham MS (2009) Layered vanadium and molybdenum oxides: batteries and electrochromics. J Mater Chem 19:2526–2552 . doi: 10.1039/B819629J

56. Przesniak-Welenc M, Karczewski J, Smalc-Koziorowska J, Lapinski M, Sadowski W, Koscielska B (2016) The influence of nanostructure size on V2O5 electrochemical properties as cathode materials for lithium ion batteries. RSC Adv 6:55689–55697 . doi: 10.1039/C6RA05695D

57. Huang S-Z, Cai Y, Jin J, Li Y, Zheng X-F, Wang H-E, Wu M, Chen L-H, Su B-L (2014) Annealed vanadium oxide nanowires and nanotubes as high performance cathode materials for lithium ion batteries. J Mater Chem A 2:14099 . doi: 10.1039/C4TA02339K

58. Kim B-H, Yang KS, Yang DJ (2013) Electrochemical behavior of activated carbon nanofiber-vanadium pentoxide composites for double-layer capacitors. Electrochimica Acta 109:859–865 . doi: 10.1016/j.electacta.2013.07.180

59. Mai L, Xu X, Han C, Luo Y, Xu L, Wu YA, Zhao Y (2011) Rational Synthesis of Silver Vanadium Oxides/Polyaniline Triaxial Nanowires with Enhanced Electrochemical Property. Nano Lett 11:4992–4996 . doi: 10.1021/nl202943b

60. Yu DM, Zhang ST, Liu DW, Zhou XY, Xie SH, Zhang QF, Liu YY, Cao GZ (2010) Effect of manganese doping on Li-ion intercalation properties of V2O5 films. J Mater Chem 20:10841 . doi: 10.1039/c0jm01252a

61. Zhu K, Qiu H, Zhang Y, Zhang D, Chen G, Wei Y (2015) Synergetic Effects of Al3+ Doping and Graphene Modification on the Electrochemical Performance of V2O5 Cathode Materials. ChemSusChem 8:1017–1025 . doi: 10.1002/cssc.201500027